NAVIGATION AND TRAJECTORY DESIGN FOR JAPANESE ACTIVE DEBRIS REMOVAL MISSION

Toru Yamamoto[(1)], **Naomi Murakami**[(1)], **Yu Nakajima**[(1)] **and Koji Yamanaka**[(1)]
[(1)]*Japan Aerospace Exploration Agency, 2-1-1 Sengen, Tsukuba, Ibaraki, 305-8505, Japan, +81-50-3362-4356, yamamoto.toru@jaxa.jp*

Abstract: *This work addresses the design of the relative navigation and the rendezvous trajectory for the Active Debris Removal (ADR) mission. The first part deals with the navigation sensor system design, whereby the characteristics of each sensor type are investigated and detectability analysis models are developed. The filter design of angles-only navigation (AON) is also presented and the observability issue of the AON is tackled in detail. Besides, the mathematical framework for rendezvous linear covariance analysis, in which the relative state is parameterized in terms of relative orbital elements, is presented. Based on relative navigation sensor analysis, a suitable trajectory design for a non-cooperative rendezvous is discussed. Finally, rendezvous simulation results are presented to demonstrate the navigation and trajectory design of the mission, and the lessons learned are discussed.*

Keywords: *Active Debris Removal, Non-cooperative Target, Angles-only Navigation.*

1. Introduction

The rising problem of space debris in orbit is a growing concern for current and future space missions. Even if all spacecraft launches were terminated today, the amount of debris would increase as a result of in-orbit collisions between objects already in orbit. Liou [1] claimed that the active removal of large and massive debris in crowded orbits can effectively to prevent the collisions which are major causes of the increasing tendency. With a good implementation of the commonly adopted mitigation measures, the Active Debris Removal (ADR) of five objects per year is supposed to stabilize the population growth. The effective target of the ADR is massive objects with high collision probabilities. Many (but not all) of the potential targets in the current environment are spent rocket upper stages.

The Japan Aerospace Exploration Agency (JAXA) studies the Electro-Dynamic Tether (EDT) system as one of the candidate devices for the ADR mission [2]. The EDT is a propulsion system that can transfer large objects and eliminates the need for propellant using interaction with the Earth's geo-magnetic field. The ADR mission to apply the EDT system for deorbiting a rocket upper stage is investigated in JAXA as one of the reference design missions. A non-cooperative rendezvous is one of the key technologies to enable the mission, since a chaser spacecraft must approach the non-cooperative target debris and attach an anchor mechanism of the tether on it.

A non-cooperative rendezvous has some difficulties compared to a conventional cooperative rendezvous (e.g. to the International Space Station). Firstly only poor preliminary knowledge of orbit is available, since the usual measures used to determine the orbit for cooperative targets such as R&RR and GNSS navigation cannot be used. Secondly a non-cooperative target lacks all navigation aids such as laser retroreflectors or markers to support reliable relative navigation. Thirdly a non-cooperative target is not controlled, meaning its attitude is in free motion in space.

A chaser spacecraft must overcome these difficulties to establish accurate and reliable relative navigation and attach the anchor mechanism to the moving target.

This work addresses the design of the relative navigation and the rendezvous trajectory for a non-cooperative rendezvous. It was mainly motivated by the ADR mission with the EDT system, which is a reference design mission investigated in JAXA. The first part of the work deals with the navigation sensor system design and there are several types of relative navigation sensors applicable to non-cooperative targets. The characteristics of each sensor types are investigated, detectability analysis models are developed and the filter design of angles-only navigation (AON) is presented. Observability is the key AON issue since instantaneous measurements lack sufficient information to reproduce a complete state vector. The observability issue of the AON is tackled depth and the mathematical framework for rendezvous linear covariance analysis, in which the relative state is parameterized in terms of relative orbital elements, is presented. Next, based on relative navigation sensor analysis, a suitable trajectory design for a non-cooperative rendezvous is discussed. Finally, rendezvous simulations are performed to demonstrate the navigation and trajectory design of the mission, and some of the lessons learned are discussed.

2. Mission Scenario

As mentioned above, the ADR mission to apply the EDT system for deorbiting a rocket upper stage is investigated in JAXA as one of the reference design missions. In this section, the mission scenario is briefly introduced and an overview of the mission is shown in Figure 1.

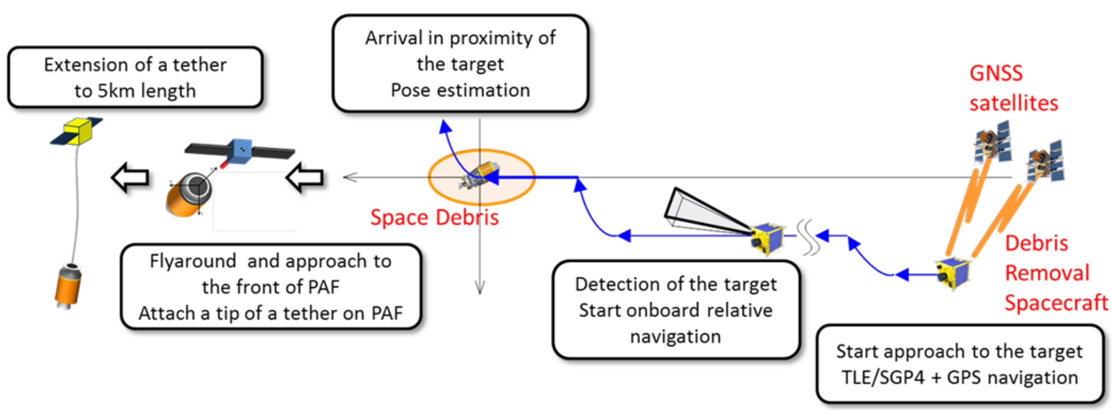

Figure 1. Scenario of the Reference ADR Mission using EDT

First of all, a chaser spacecraft begins to approach using preliminary orbit information of the target as its primary absolute navigation source. Since the usual measures to determine spacecraft orbit such as R&RR and GPS cannot be used for the debris, the preliminary orbit information relies on ground-based radar tracking such as Two-Line Elements (TLEs) provided by JSpOC. Onboard realtime GNSS navigation can be used to identify the primary absolute navigation source of the chaser spacecraft.

The chaser spacecraft approaches to the target so that the dispersions of estimated target position can be covered with the field-of-view (FOV) of onboard relative navigation sensors. Subsequently the relative navigation sensors detect the target, collect measurements, and the onboard navigation filter refines relative navigation accuracy. If camera-type relative navigation sensors are used, the target is imaged as a tiny dot at the moment. Therefore only Line-Of-Sight (LOS) angles can be extracted as meaningful information. Hence Angles-Only Navigation (AON) is considered as the primary navigation method during far-range rendezvous phase.

As the chaser approaches, the apparent target size expands. When the relative distance reaches one km, the apparent size becomes sufficiently large to measure the relative distance directly from the images obtained by the camera-type sensor. From this distance, the primary navigation method is switched from the AON to the Model-Matching Navigation (MMN), which estimates the position and attitude relative to the target by correlating the images obtained with the known target 3D shape information. The chaser spacecraft approaches the target along the V-bar and stops at the 30 m hold point.

At the 30 m hold point on the V-bar, consecutive images of the target are collected and its actual condition is investigated, while precise pose estimation and prediction is performed by these images on-ground and the proper final approach trajectory is generated with reference to the predicted motion of the Payload Attach Fitting (PAF) of the target rocket upper stage.

The chaser spacecraft departs from the 30 m hold point and moves along the pre-generated trajectory to the front of the PAF, whereupon the PAF-Tracking Navigation (PTN) is initiated. The PTN estimates the relative position and attitude with respect to the PAF surface from images obtained in realtime, guidance logic is then switched from MMN- to PTN-based guidance and the chaser spacecraft descents to the hold position located in the vicinity of the center of the PAF ring and controls the relative position and attitude so that the chaser spacecraft stands still with respect to the PAF meanwhile. After the situation has been confirmed by ground operators, the EDT system anchor mechanism is attached to the PAF, and the chaser spacecraft departs from the target to extend the tether properly.

3. Absolute Navigation by TLE/SGP4

One of the difficulties encountered in the non-cooperative rendezvous is the poor preliminary orbit knowledge of the target. The most common information source of the space debris orbit is TLEs provided by JSpOC. To generate ephemeris from TLEs, SGP4 is usually used as the propagator. The accuracy of the predicted ephemeris generated from TLE/SGP4 is affected by atmospheric density in the upper atmosphere and thus it depends orbital altitude and solar activity on the day. To comprehend the typical performance for the target space debris, the accuracy of the TLE/SGP4 of the ADEOS-II satellite is investigated. Figure 2 shows an example of the evaluation results. ADEOS-II is a Japanese Earth observation satellite which was launched in 1996 and which flies in an 800 km sun-synchronous orbit; allowing it to effectively exemplify this performance evaluation since a sun-synchronous orbit at an altitude of 800 km is one of the most crowded orbits where many effective potential ADR targets exist. The TLE/SGP4 performance is evaluated by adopting onboard GPS navigation solutions as the reference.

Even tangential errors become larger as time goes by from epoch, it remains within 2 km for 4 days, while both radial and cross-track errors are about 500m – 1km and do not grow significantly over time. The updating cycle of the target debris TLE by JSpOC cannot be controlled, but usually exceeds 4 days, meaning it may be feasible to approach the target up to 10 - 20 km of tangential distance separation using TLE/SGP4 as the primary navigation source.

In addition, other radar tracking stations can also be used and Japan also houses a radar tracking station at Kamisaibara which can track and generate TLE of space debris in Low-Earth Orbit (LEO) [3]. DLR reported the orbit prediction accuracy achievalbe by the TIRA radar tracking facility for relative navigation to non-cooperative targets in LEO [4]. If such radar tracking stations are available, fresh TLEs can be provided for critical events of the rendezvous mission operation.

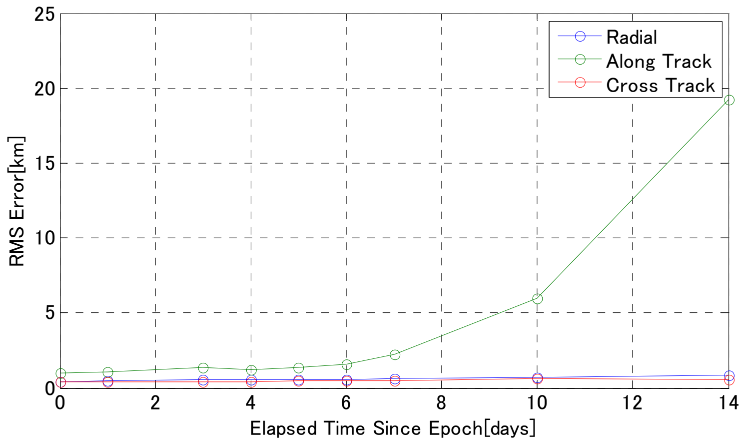

Figure 2. ADEOS-II TLE/SGP4 accuracy vs. elapsed time since epoch, May 2003.

4. Relative Navigation Sensor

4.1 Navigation Sensor for Non-Cooperative Rendezvous

A non-cooperative target has no navigation aids such as radio transmitters, GPS receivers, laser retroreflectors, and markers, meaning the applicable relative navigation sensors differ from those of cooperative rendezvous missions. The types of applicable navigation sensors for a non-cooperative rendezvous are listed in Table 1.

Table 1. Navigation Sensor Types

		Attitude	Range		LOS Angles	Night	Pros	Cons
			Far	Near				
Visible Camera		✓	NG	✓	✓	NG	Low cost Avaliable at long distance High resolution	Not available during eclipse Sensitive to lighting conditions Poor range accuracy
Infrared Camera		✓	NG	✓	✓	✓	Low cost Available during eclipse Robust to lighting conditions	Low resolution Poor range accuracy
Laser Sensor	LIDAR (Range only)	NG	✓	✓	NG	✓	Available during eclipse Available at long distance High range accuracy	Expensive LOS angles not measured Expensive
	Scanning LIDAR	✓	✓	✓	✓	✓	Available during eclipse Avalialbe at long distance High range accuracy Pose estimation capability	Very Expensive
	Flash LIDAR	✓	NG	✓	✓	✓	Available during eclipse Pose estimation capability	Expensive

Since a visible camera (VISCAM) utilizes strong sunlight as an illuminator, it can detect targets from great distances in the event of optimal lighting conditions, optical properties of the targets, and the angle of the target surface to the LOS of the camera. According to the Orbital Express experiment, the farthest distance where VISCAM could detect the target was about 500 km [5]. However it is not available during an eclipse. Moreover, it is sensitive and not robust to lighting condition variations.

Conversely, an infrared thermal camera (IRCAM) is available even during an eclipse. Besides, it is robust against lighting condition variations, because the sensitive wavelength range (8 – 14 μm) has no overlap with that of sunlight. This means an IRCAM can be a very effective navigation measure for a non-cooperative rendezvous.

A LIDAR may also be applicable for non-cooperative targets. It transmits a laser beam, receives the reflected light, and computes the relative range between the sensor and target. A LIDAR can be categorized into three types. One is a type which can only measure range. Another is a scanning LIDAR, which swings narrow laser beams mechanically and measures not only range but also LOS angles. The other is a flash LIDAR, which transmits laser pulses diffused in wide field-of-view (FOV), and receives return pulses with a 2D array detector and can also measure range and LOS angles. The strong point of the LIDAR compared with the VISCAM and IRCAM is its ability directly obtain range information. Furthermore using a scanning or flash LIDAR enables pose estimation by matching 3D point cloud data with a known 3D model of the target. Conversely, a spaceborne LIDAR is generally expensive and it is the weak point.

4.2 Navigation Sensor Model to Analyze Detectability

For quantitative analysis of a non-cooperative rendezvous, it is important to know the available range limit of the relative navigation sensor. For this purpose, a navigation sensor detectability model is developed for each sensor type. Figure 3 shows a comprehensive illustration of how the navigation sensor detectability is modeled.

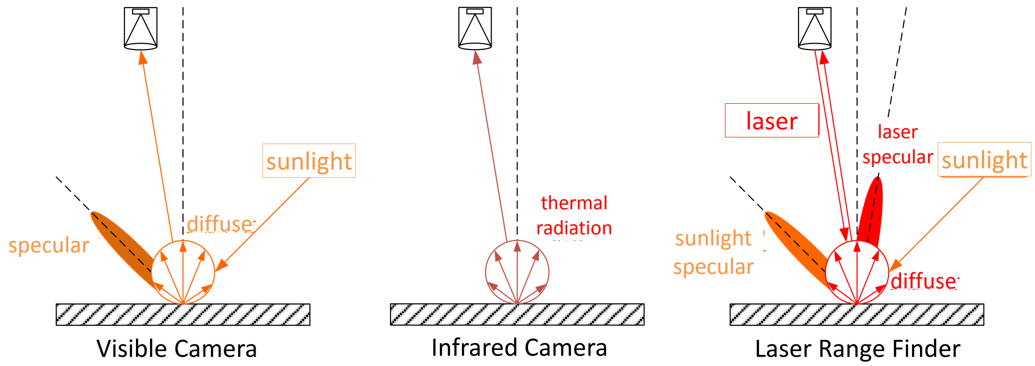

Figure 3. Illustration of the Navigation Sensor Detectability Model

A VISCAM utilizes strong sunlight as an illuminator. An IRCAM detects infrared radiation from the target itself. It does not have sensitivity in the sunlight wavelength range. A LIDAR transmits a laser beam and receives its return. Usually laser wavelength is near infrared ray (0.8 – 1.6 µm) so that the reflectance of sunlight may be disruptive.

Radiance of the reflected visible light is modeled as follows:

$$L = f_{BRDF} E \cos(\theta_i) \tag{1}$$

where f_{BRDF} is a Bidirectional Reflectance Distribution Function (BRDF), E is the irradiance of the radiated visible light, and θ_i is the incident angle. If the input visible light is a laser beam from a LIDAR, E is the irradiance of the incoming laser beam. As a BRDF, the following modified Phong model is used [6] :

$$f_{BRDF} = \frac{k_d}{\pi} + \frac{k_s(n+2)}{2\pi} \cos^n(\alpha) \tag{2}$$

where k_d is the diffuse reflectivity, k_s the specular reflectivity, n the specular exponent, and α the angle between the perfect specular reflective direction and the outgoing direction. The reflectivity coefficients should be set keeping the relationship of $k_d + k_s \leq 1$ for energy conservation.

Radiance of infrared radiation from the target is modeled as follows:

$$L = \epsilon \int_{8\mu m}^{14\mu m} L_\lambda(T, \lambda) d\lambda \tag{3}$$

where ϵ is the infrared emissivity of the material, L_λ is the spectral radiance of a black body, T is the temperature of the target, and λ is the wavelength.

The signal-to-noise ratio (SN) of a VISCAM can be computed by

$$P_r = L \cdot A\cos(\theta_o) \cdot 4\pi \frac{\pi(D/2)^2}{4\pi r^2} \cdot \tau_r \tag{4}$$

$$V_s = K_v \cdot K_{CCD} \cdot \Delta t \cdot P_r \tag{5}$$

$$SN_{VISCAM} = V_S / V_N \tag{6}$$

where P_r is the received power, A is the target area, θ_o is the angle between the target surface normal vector and the LOS vector, D is the effective diameter of optics, r is the distance, τ_r is the transmittance of optics, K_v is the CCD gain, K_{CCD} is the CCD sensitivity, Δt is the exposure time, V_S is the signal voltage, and V_N is the noise voltage. If the SN exceeds 10, the target is detectable.

The SN of an IRCAM can be computed as follows:

$$SN_{IRCAM} = P_r / NEP_f \tag{7}$$

where, P_r is the received power which can be also computed by Eq. (4), and NEP_f is the noise equivalent power of the detector.

The SN of a LIDAR can be computed as follows:

$$P_r = L \cdot A(r) \cdot cos(\theta_o) \cdot 4\pi \frac{\pi(D/2)^2}{4\pi^2} \cdot \tau_r \tag{8}$$

$$A(r) = \begin{cases} \pi \left(\frac{r\Delta\theta}{2}\right)^2 & (if\ target\ is\ smaller\ than\ laser\ spot) \\ \\ A_0 & (if\ target\ is\ larger\ than\ laserspot) \end{cases} \tag{9}$$

$$P_N = \sqrt{2e\frac{P_r + P_B}{S_A}B + NEP^2 \cdot B} \tag{10}$$

$$SN_{LIDAR} = P_r / P_N \tag{11}$$

where, P_r is the received power which can also be computed by Eq. (4), $\Delta\theta$ is the divergence angle of a laser beam, e is the elementary charge, P_B is the background power, S_A is the sensitivity of the detector, B is the bandwidth, and NEP is the noise equivalent power of the detector. The effective target area $A(r)$ should be computed considering the relationship between the target size and the size of the laser spot.

Figure 4 shows an example of the computed SN for each type of navigation sensor. The target is modeled as a flat plate with $k_d = 0.2, k_s = 0.5, n = 28$ and the parameters of navigation sensors are set referring to the specifications of existing spaceborne or commercial products.

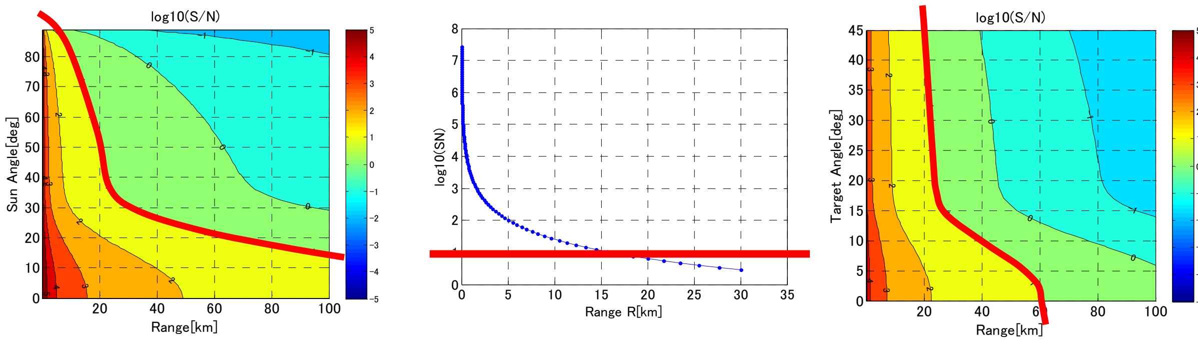

Figure 4. An Example of Sensor Detectability Analysis (left: VISCAM SN vs. range and θ_i, middle: IRCAM SN vs. range, right: LIDAR SN vs. range and θ_o, red bold line is SN = 10)

As seen in Figure 4 (left), the SN of the VISCAM is strongly affected by the sunlight incident angle θ_i. If the sun is located right behind of the VISCAM ($\theta_i = 0$ deg), it can receive strong specular reflection from the target, which means its detectability can be retained, even with very long relative distance. Conversely, if the sun is located just beside of the VISCAM ($\theta_i = 90$ deg), it can receive only faint diffuse reflection and the available range is limited.

Conversely, the SN of the VISCAM (middle) does not depend on the existence of sunlight, which means its detectability is expected to be robust against illumination conditions. Note that although the target temperature is considered constant in this work, the actual temperature of the target in orbit varies periodically, which should be kept in mind for more detailed analysis.

As seen in Figure 4 (right), the SN of the LIDAR is strongly affected by the angle between the target surface normal vector and the LOS vector. If both vectors are parallel ($\theta_o = 0$ deg), it can receive strong specular reflection from the transmitted laser beam. If the target surface normal vector differs significantly from the LOS vector, the specular reflection component goes away to space and only the faint diffuse reflection component can reach the LIDAR receiver.

As described above, the developed detectability model captures the essential characteristics of each type of navigation sensor and is used to compute detectability for non-cooperative rendezvous simulations described later.

4.3 Navigation Sensor Usage Matrix

Considering the above discussion, the preferable design of the navigation sensor usage matrix for the reference mission is studied and a chart shows which navigation sensor is used as the primary navigation source at each relative range. Figure 5 shows the result.

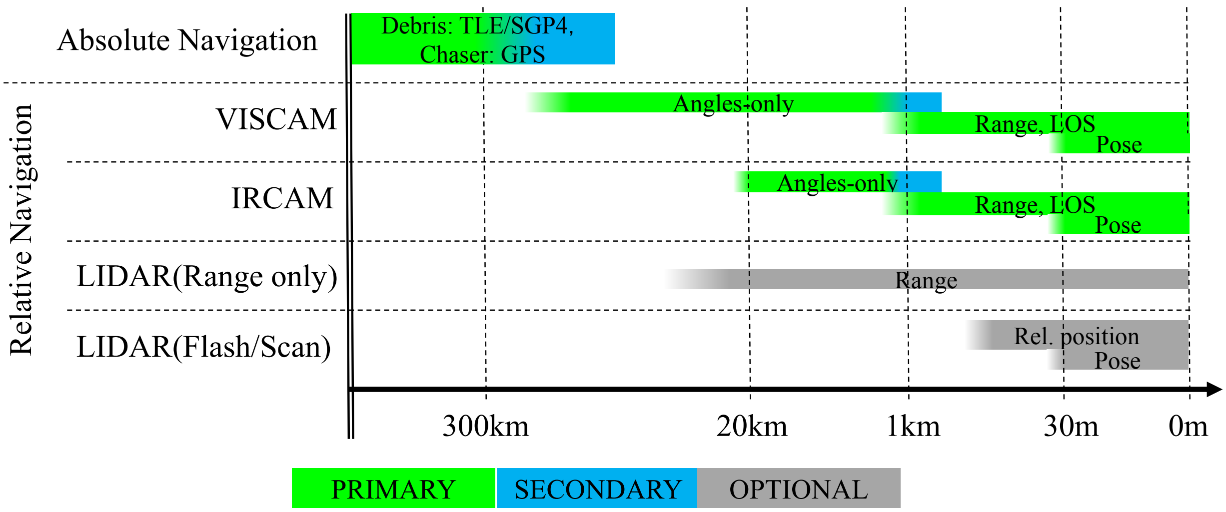

Figure 5. Navigation Sensor Usage Matrix for the Reference Mission

First of all, the chaser spacecraft begins to approach using TLE/SGP4 navigation for the target and onboard GNSS navigation for the chaser.

Subsequently, the VISCAM detects the target and starts collecting measurements and the target detection by VISCAM is to be achieved within the range 100 km or more, while the primary navigation source is switched to the AON using VISCAM measurements. The measurements are currently intermittent and are not available at the orbital location of eclipses or when the sun is in the wrong dierction.

The IRCAM is expected to detect the target at around 20 km, whereupon the AON begins to incorporate the IRCAM measurements into its navigation filter, from where measurements are always available regardless of eclipses and the sun direction.

At around 1 km, the apparent target size becomes sufficient to perform model-matching based on image processing. From here, the MMN is initiated to provide range and LOS measurements. THe MMN uses both of the VISCAM and IRCAM measurements. Meanwhile the AON and MMN are carried out in parallel. Once the MMN check-out is completed, the primary navigation source is switched to the MMN.

The baseline design for the navigation sensor system accommodates only the VISCAM and the IRCAM. Even though the LIDAR appeals with its ability to provide direct range information, it is recognized as an optional alternative due to its cost.

5. Angles-Only Navigation

5.1 Overview of Angles-Only Navigation

When the distance between the chaser and target is far, the target is imaged by a camera-type sensor as a tiny dot. Under these circumstances, range information cannot be obtained but only LOS angles can be extracted as meaningful information from a measurement. The AON, which is the navigation method used to reproduce complete state vectors using only LOS angles measurements, is recognized as an important navigation technique for non-cooperative rendezvous missions, and is expected to be the primary relative navigation source during the far-range rendezvous phase. One essential challenge of the AON is the inherent difficulty in acquiring the relative range to the target using only LOS angles information. Observability is the key issue of the AON since instantaneous measurements lack sufficient information to reproduce a complete state vector. In view of the emerging needs for a non-cooperative rendezvous, several authors have recently contributed to facilitate understanding of AON observability.

Woffinden, et al. [7] claimed that a relative state vector is not observable by processing LOS angle measurements of natural relative orbit and modeling relative motion by the linearized CW equation [8] on the orthogonal Hill coordinate. In addition it is demonstrated that a maneuver which triggers a change in the natural LOS angle trend can make the system observable, including the along-track separation. Another work by Woffinden, et al. [9] introduced criteria to determine optimal maneuvering and stimulate observability as much as possible.

Gaias. et al. [10] presented the formulation of the AON relative navigation filter, which utilizes relative orbital elements as a state vector. Simple metrics of observability by examining the condition number of a measurement mapping matrix are introduced. Moreover, alghough the natural relative orbit, as modeled by the Keplerian-based state-transition matrix (STM), does not make the system observable, faint observability is generated if it is modeled by the J2-included STM. A simple way to determine a maneuver to maximize enhancement of observability is also presented.

In this work, it is shown that processing LOS angle measurements of natural relative orbit can actually make the system observable when coordinate transformation between orthogonal frame and curvilinear frame is properly modeled, which is explained from both intuitive and numerical perspectives. A modified AON relative navigation filter formulation is proposed, which includes proper treatment of the coordinate transformation. Furthermore, the properly scaled condition number of a measurement mapping matrix is introduced as a useful tool to assess observability. The key characteristic of observability for natural relative motion, which is clear relationship between observability and relative distance, is also presented.

5.2 Nonlinear Truth Model

This section introduces a truth model, which provides the true states and measurements. Figure 1 shows definitions of the LOS angles and coordinate systems.

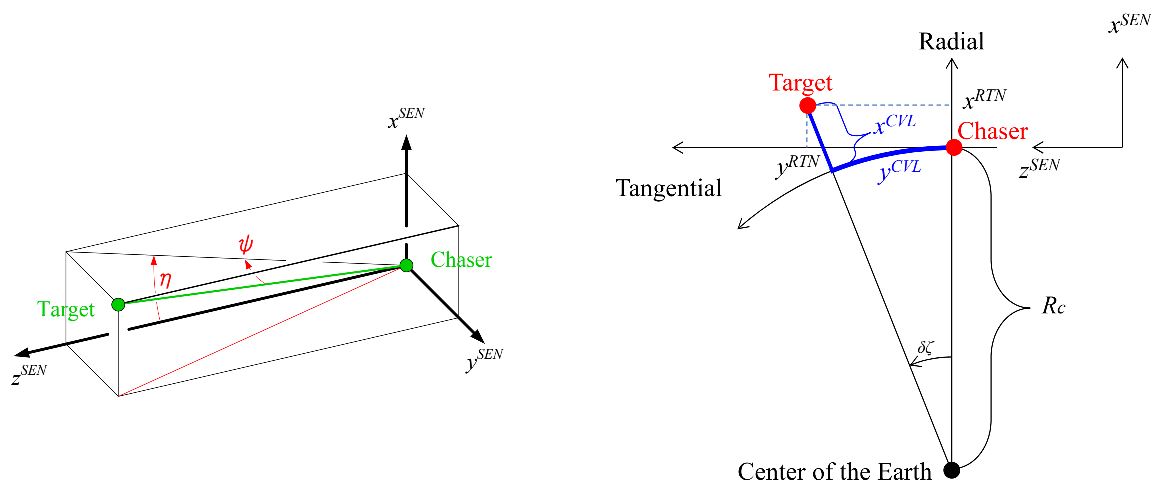

Figure 6. Definition of LOS angles (left) and RTN/CVL/SEN coordinate system (right)

A camera-type navigation sensor provides two LOS angles as measurements : elevation η and azimuth ψ . As shown in Fig. 6, η represents a LOS angle due to in-plane motion, and ψ represents a LOS angle due to out-of-plane motion.

The radial-tangential-normal (RTN) coordinate is an orthogonal coordinate frame; the origin of which is located at the chaser spacecraft position. The curvilinear (CVL) coordinate is a cylindrical coordinate frame, with a y-axis bent along a circular orbit, while the sensor (SEN) coordinate is an orthogonal coordinate frame fixed with a navigation sensor. The CW equation is not linearized on the RTN frame but on the CVL frame. Conversely, a camera-type navigation sensor measures LOS angles in the SEN frame, which is the key difference allowing the AON to be observed.

The time-update equation of the position and velocity of both the chaser and target is as follows:

$$\begin{pmatrix} \dot{\boldsymbol{r}}^{ECI} \\ \dot{\boldsymbol{v}}^{ECI} \end{pmatrix} = \begin{pmatrix} \boldsymbol{v}^{ECI} \\ \boldsymbol{f}(t, \boldsymbol{r}^{ECI}, \boldsymbol{v}^{ECI}) \end{pmatrix} \tag{12}$$

where ECI means the Earth-centered inertia coordinate frame, and $\boldsymbol{f}$ is the nonlinear acceleration model for orbit propagation. The true LOS angle measurements are computed by the unit vector to the target in the SEN coordinate frame $\boldsymbol{u}^{SEN}$ as follows:

$$\boldsymbol{z}^{CAM} = \begin{pmatrix} \eta \\ \psi \end{pmatrix} = \boldsymbol{h}^{CAM} + \boldsymbol{\nu}^{CAM} = \begin{pmatrix} \mathrm{atan2}(u_x^{SEN}, u_z^{SEN}) \\ \mathrm{asin}(u_y^{SEN}) \end{pmatrix} + \boldsymbol{\nu}^{CAM} \tag{13}$$

$$\begin{gathered} \boldsymbol{u}^{SEN} = (\delta r_x^{SEN} \quad \delta r_y^{SEN} \quad \delta r_z^{SEN})^T / \delta r \\ \delta r = \sqrt{\delta r_x^{SEN\,2} + \delta r_y^{SEN\,2} + \delta r_z^{SEN\,2}} \end{gathered} \tag{14}$$

where δ denotes the relative value of the target with respect to the chaser, $\boldsymbol{\nu}^{CAM}$ is the random measurement noise, and δr^{SEN} is the relative position in the SEN frame. In this work, the relationship between SEN and RTN frames is considered constant:

$$\delta \boldsymbol{r}^{SEN} = \boldsymbol{C}_{RTN}^{SEN} \delta \boldsymbol{r}^{RTN} \tag{15}$$

$$\boldsymbol{C}_{RTN}^{SEN} = \begin{pmatrix} 1 & 0 & 0 \\ 0 & 0 & -1 \\ 0 & 1 & 0 \end{pmatrix} \tag{16}$$

The relative position in the RTN frame $\delta \boldsymbol{r}^{RTN}$ can be computed from the absolute position and velocity vectors as follows:

$$\begin{aligned} \boldsymbol{u}_R^{RTN} &= \frac{\boldsymbol{r}_c^{ECI}}{\|\boldsymbol{r}_c^{ECI}\|} \\ \boldsymbol{u}_N^{RTN} &= \frac{\boldsymbol{r}_c^{ECI} \times \boldsymbol{v}_c^{ECI}}{\|\boldsymbol{r}_c^{ECI} \times \boldsymbol{v}_c^{ECI}\|} \\ \boldsymbol{u}_T^{RTN} &= \boldsymbol{u}_N^{RTN} \times \boldsymbol{u}_R^{RTN} \\ \boldsymbol{C}_{ECI}^{RTN} &= (\boldsymbol{u}_R^{RTN}, \boldsymbol{u}_T^{RTN}, \boldsymbol{u}_N^{RTN})^T \\ \delta \boldsymbol{r}^{RTN} &= \boldsymbol{C}_{ECI}^{RTN} (\boldsymbol{r}_t^{ECI} - \boldsymbol{r}_c^{ECI}) \end{aligned} \tag{17}$$

where subscript c denotes the chaser and t denotes the target. As described in Eqs. (13) – (17), the true LOS angle measurements are computed without any linearization.

Similarly, the true range measurement of the LIDAR is computed as follows:

$$z^{LIDAR} = h^{LIDAR} + \nu^{LIDAR} = \delta r + \nu^{LIDAR} \tag{18}$$

The truth value of the relative orbital elements can also be computed from the absolute position and velocity vectors. The definition of the relative orbital element (ROE) is [10]:

$$\delta \boldsymbol{\alpha}(\boldsymbol{e}_t^{mean}, \boldsymbol{e}_c^{mean}) = \begin{pmatrix} \delta a \\ \delta e \cos\varphi \\ \delta e \sin\varphi \\ \delta i \cos\theta \\ \delta i \sin\theta \\ \delta u \end{pmatrix} = \begin{pmatrix} \dfrac{a_t - a_c}{a_c} \\ e_t \cos\omega_t - e_c \cos\omega_c \\ e_t \sin\omega_t - e_c \sin\omega_c \\ i_t - i_c \\ (\Omega_t - \Omega_c)\sin i_c \\ u_t - u_c \end{pmatrix} \tag{19}$$

where $\boldsymbol{e}$ is represents classical orbital elements, a is the semimajor axis, e is eccentricity, i is inclination, u is the argument of latitude, Ω is the right ascension of ascending node, and mean denotes mean orbital elements. The classical orbital elements are defined as:

$$\boldsymbol{e} = (a, e_x, e_y, i, \Omega, u)^T \tag{20}$$

where e_x and e_y are eccentricity vector components. The osculating orbital elements can be computed by absolute position and velocity vectors:

$$\boldsymbol{e}^{osc} = rv\_to\_osc(\boldsymbol{r}^{ECI}, \boldsymbol{v}^{ECI}) \tag{21}$$

where $rv\_to\_osc()$ is the function to compute classical orbital elements from the ECI position and velocity vectors. By subtracting short-period perturbations due to the J2 term, the mean orbital elements can be computed :

$$\boldsymbol{e}^{mean} = osc\_to\_mean(\boldsymbol{e}^{osc}) \tag{22}$$

where $osc\_to\_mean()$ denotes a function to compute the mean orbital element. Using Eqs. (19) - (22), the true ROE can be obtained.

5.2 Linearized Model for Onboard Navigation

This section presents the formulation of the onboard navigation filter. The formulation of the AON navigation filter is based on that of Gaias. et al. [10] with some added modifications. The state vector is defined as:

$$\boldsymbol{x} = a_c \delta\boldsymbol{\alpha} \tag{23}$$

For time-update, the following linearized STM is used:

$$\boldsymbol{\Phi}(t_{k+1}, t_k) = \begin{pmatrix} 1 & 0 & 0 & 0 & 0 & 0 \\ 0 & 1 & -\dot{\varphi}\Delta t & 0 & 0 & 0 \\ 0 & \dot{\varphi}\Delta t & 1 & 0 & 0 & 0 \\ 0 & 0 & 0 & 1 & 0 & 0 \\ 0 & 0 & 0 & 3\gamma \sin^2(i)\, n\Delta t & 1 & 0 \\ -1.5n\Delta t & 0 & 0 & -12\gamma \sin(2i)\Delta t & 0 & 1 \end{pmatrix} \tag{24}$$

$$\Delta t = t_{k+1} - t_k$$

The time-update of the estimated state vector $\hat{\boldsymbol{x}}$ and its covariance matrix is $\hat{P}$ as follows:

$$\hat{\boldsymbol{x}}_{k+1} = \boldsymbol{\Phi}\hat{\boldsymbol{x}}_k$$
$$\hat{\boldsymbol{P}}_{k+1} = \boldsymbol{\Phi}\hat{\boldsymbol{P}}_k\boldsymbol{\Phi}^T + \boldsymbol{Q}\Delta t \tag{25}$$

where $\boldsymbol{Q}$ is the process noise covariance matrix. Measurement-update is done by the standard EKF formulation:

$$\hat{x}_k^+ = \hat{\boldsymbol{x}}_k^- + \boldsymbol{K}\big(\boldsymbol{z} - \hat{\boldsymbol{h}}(\hat{\boldsymbol{x}}_k^-, t_k)\big)$$
$$\hat{\boldsymbol{P}}_k^+ = (\boldsymbol{I} - \boldsymbol{K}\boldsymbol{H})\hat{\boldsymbol{P}}_k^- \tag{26}$$

$$\boldsymbol{K} = \hat{\boldsymbol{P}}_k^- \boldsymbol{H}^T\big(\boldsymbol{H}\hat{\boldsymbol{P}}_k^- \boldsymbol{H}^T + \boldsymbol{R}\big)^{-1} \tag{27}$$

The measurement model of the camera-type sensor is:

$$\hat{\boldsymbol{h}}^{CAM}(\hat{\boldsymbol{x}}_k^-, t_k) = \begin{pmatrix} \mathrm{atan2}(\hat{u}_x^{SEN}, \hat{u}_z^{SEN}) \\ \mathrm{asin}(\hat{u}_y^{SEN}) \end{pmatrix} \tag{28}$$

while that of the LIDAR type sensor is:

$$\hat{h}^{LIDAR}(\hat{\boldsymbol{x}}_k^-, t_k) = \delta\hat{r} \tag{29}$$

Compared with the truth model, in the onboard navigation filter formulation, the modeled measurement is computed by the ROE instead of the absolute position and velocity in the ECI frame. The relative position in the SEN frame is computed as follows:

$$\delta\hat{\boldsymbol{r}}^{SEN} = \boldsymbol{C}_{RTN}^{SEN}\boldsymbol{c}_{CVL}^{RTN}(\boldsymbol{C}_{ROE}^{CVL}\ \hat{\boldsymbol{x}}_k^-) \tag{30}$$

where $\boldsymbol{C}_{ROE}^{CVL}$ is the coordinate transformation matrix from ROE to the relative position in the CVL frame:

$$\boldsymbol{C}_{ROE}^{CVL} = \frac{\partial\delta\boldsymbol{r}^{CVL}}{\partial a_t \delta\boldsymbol{\alpha}} = \begin{pmatrix} 1 & -\cos u & -\sin u & 0 & 0 & 0 \\ 0 & 2\sin u & -2\cos u & 0 & \cot i & 1 \\ 0 & 0 & 0 & \sin u & -\cos u & 0 \end{pmatrix} \tag{31}$$

Note that $\boldsymbol{C}_{ROE}^{CVL}$ is not the coordinate transformation matrix to the RTN frame but to the CVL frame. $\boldsymbol{c}_{CVL}^{RTN}$ is a function to map the position vector in the CVL frame into the RTN frame as shown in Figure 6:

$$\boldsymbol{c}_{CVL}^{RTN}(\delta\hat{\boldsymbol{r}}^{CVL}) = \begin{pmatrix} \delta\hat{r}_x^{CVL}\cos\big(\delta\hat{\xi}\big) - R_c\Big(1 - \cos\big(\delta\hat{\xi}\big)\Big) \\ (R_c + \delta\hat{r}_x^{CVL})\sin\big(\delta\hat{\xi}\big) \\ \delta\hat{r}_z^{CVL} \end{pmatrix}$$
$$\delta\hat{\xi} = \frac{\delta\hat{r}_y^{CVL}}{R_c} \tag{32}$$

The measurement matrices of the camera-type and the LIDAR type sensors are obtained by partial derivatives of the measurement models:

$$\boldsymbol{H}^{CAM} = \frac{\partial \hat{\boldsymbol{h}}^{CAM}}{\partial \boldsymbol{x}} = \begin{pmatrix} \frac{\partial \eta}{\partial \delta \boldsymbol{r}^{SEN}} & \frac{\partial \psi}{\partial \delta \boldsymbol{r}^{SEN}} \end{pmatrix}^T \boldsymbol{C}_{RTN}^{SEN} \boldsymbol{C}_{CVL}^{RTN} \boldsymbol{C}_{ROE}^{CVL} \tag{33}$$

$$\boldsymbol{H}^{LIDAR} = \frac{\partial \hat{h}^{LIDAR}}{\partial \boldsymbol{x}} = \frac{\partial \delta r}{\partial \delta \boldsymbol{r}^{SEN}} \boldsymbol{C}_{RTN}^{SEN} \boldsymbol{C}_{CVL}^{RTN} \boldsymbol{C}_{ROE}^{CVL} \tag{34}$$

$$\begin{gathered} \frac{\partial \eta}{\partial \delta \boldsymbol{r}^{SEN}} = \frac{1}{\delta r \cos^2(\psi)} \left(\frac{\partial \boldsymbol{u}^{SEN}}{\partial \eta} \right)^T = \frac{1}{\delta r \cos^2(\psi)} \begin{pmatrix} \cos(\psi)\cos(\eta) \\ 0 \\ -\cos(\psi)\sin(\eta) \end{pmatrix} \\ \frac{\partial \psi}{\partial \delta \boldsymbol{r}^{SEN}} = \frac{1}{\delta r} \left(\frac{\partial \boldsymbol{u}^{SEN}}{\partial \psi} \right)^T = \frac{1}{\delta r} \begin{pmatrix} -\sin(\psi)\sin(\eta) \\ \cos(\psi) \\ -\sin(\psi)\cos(\eta) \end{pmatrix} \end{gathered} \tag{35}$$

$$\frac{\partial \delta r}{\partial \delta \boldsymbol{r}^{SEN}} = \begin{pmatrix} \delta r_x^{SEN} & \delta r_y^{SEN} & \delta r_z^{SEN} \end{pmatrix} / \delta r \tag{36}$$

The difference in formulation with respect to that of Gaias. et al. [10] is the addition of the coordinate transformation matrix $\boldsymbol{C}_{CVL}^{RTN}$. which is obtained by partial derivatives of the function $\boldsymbol{c}_{CVL}^{RTN}$ as follows:

$$\boldsymbol{C}_{CVL}^{RTN} = \frac{\partial}{\partial \delta \boldsymbol{r}^{CVL}} \boldsymbol{c}_{CVL}^{RTN}(\delta \hat{\boldsymbol{r}}^{CVL}) = \begin{pmatrix} \cos(\delta\hat{\xi}) & -\left(1 + \frac{\delta \hat{r}_x^{CVL}}{R_c}\right) \sin\left(\delta\hat{\xi}\right) & 0 \\ \sin\left(\delta\hat{\xi}\right) & \frac{R_c + \delta \hat{r}_x^{CVL}}{R_c} \cos\left(\delta\hat{\xi}\right) & 0 \\ 1 & 0 & 1 \end{pmatrix} \tag{37}$$

At this stage, all necessary equations to compute the measurement models $\boldsymbol{h}$ and the measurement matrices $\boldsymbol{H}$ are ready.

When an impulse orbital maneuver is performed, some corrections are added to the estimated state vector and its covariance as follows:

$$\begin{gathered} \hat{\boldsymbol{x}}_k^+ = \hat{\boldsymbol{x}}_k^- + \boldsymbol{B}\, \Delta \boldsymbol{v}^{RTN} \\ \hat{\boldsymbol{P}}_k^+ = \hat{\boldsymbol{P}}_k^- + \boldsymbol{B} \boldsymbol{S}_v \boldsymbol{B}^T \end{gathered} \tag{38}$$

where $\boldsymbol{S}_v$ is the maneuver noise matrix and $\boldsymbol{B}$ is the mapping function to compute the variation in ROE caused by the impulsive maneuver:

$$
\boldsymbol{B} = -\frac{1}{n}\begin{pmatrix} 0 & 2 & 0 \\ \sin(u_c) & 2\cos(u_c) & 0 \\ -\cos(u_c) & 2\sin(u_c) & 0 \\ 0 & 0 & \cos(u_c) \\ 0 & 0 & \sin(u_c) \\ -2 & 0 & -\sin(u_c)\cot(i_c) \end{pmatrix} \tag{39}
$$

5.2 Observability Analysis

Observability is the key issue of the AON since instantaneous measurements lack sufficient information to reproduce a complete state vector. Processing LOS angle measurements of natural relative orbit can make the system observable when the coordinate transformation between the orthogonal RTN and CVL frames is properly modeled.

There are infinite similar solutions comprising relative orbits to reproduce the same LOS angle measurement profiles as seen in Figure 7 (left), which means it seems impossible to determine the unique relative orbit using LOS angle measurement profiles, rendering the system not observable. However, the CW equations are actually linearized with respect to the curvilinear CVL coordinate frame, whereas the LOS angles are measured in the orthogonal RTN frame. This means similar solutions of relative orbits obtained by CW equations in the CVL frame are not similar when mapped into the RTN frame. Consequently, these similar relative orbits can be distinguished and their unique relative orbit can be determined by the LOS angle measurements as shown in Figure 7 (right), which means the system is actually observable.

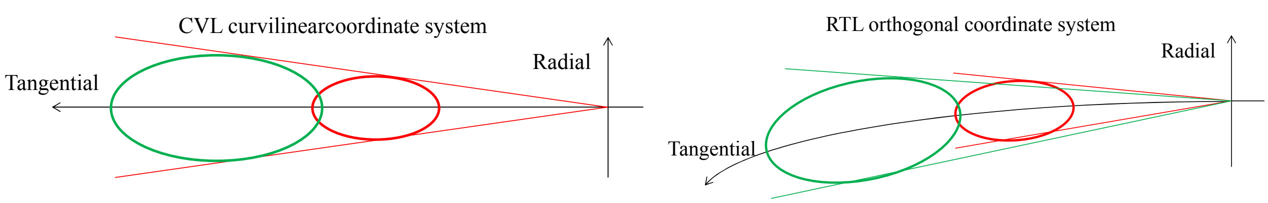

Figure 7. Similar Relative Orbits of the CW equation as seen in CVL (left) and RTN (right)

Henceforth, a useful tool to assess observability is introduced. The estimation problem of the AON can be written as follows:

$$
\boldsymbol{b} = \boldsymbol{A}\boldsymbol{x}(t_0) + \boldsymbol{n} \tag{40}
$$

$$
\boldsymbol{b} = \begin{pmatrix} \boldsymbol{z}^{CAM}(t_0) \\ \vdots \\ \boldsymbol{z}^{CAM}(t_n) \end{pmatrix}, \boldsymbol{A} = \begin{pmatrix} \boldsymbol{H}(t_0)\boldsymbol{\Phi}(t_0, t_0) \\ \vdots \\ \boldsymbol{H}(t_n)\boldsymbol{\Phi}(t_n, t_0) \end{pmatrix}, \boldsymbol{n} = \begin{pmatrix} \boldsymbol{\nu}(t_0) \\ \vdots \\ \boldsymbol{\nu}(t_n) \end{pmatrix} \tag{41}
$$

If the measurement mapping matrix $\boldsymbol{A}$ is full-rank, the system is observable since its inverse matrix $\boldsymbol{A}^{-1}$ can be computed and the state can be estimated by the least-squares method. As Gaias. et al. [10] presented, observability can be assessed by examining the condition number of $\boldsymbol{A}$. It should be noted that the measurement mapping matrix should be properly normalized to adjust the scaling of each measurement and state as follows [11]:

$$\boldsymbol{b}' = \boldsymbol{N}^{-\frac{1}{2}}\boldsymbol{b}$$

$$\boldsymbol{A}' = \boldsymbol{N}^{-\frac{1}{2}}\boldsymbol{A}\boldsymbol{D}^{-1} \tag{42}$$

$$\boldsymbol{x}' = \boldsymbol{D}\boldsymbol{x}$$

where $\boldsymbol{N} = \boldsymbol{E}[\boldsymbol{n}\boldsymbol{n}^T]$ is the matrix to normalize measurements. It is not important for the case of the AON, since both η and ψ are supposed to have equivalent noises. $\boldsymbol{D}$ is a diagonal $n \times n$ matrix with elements equal to the l_2 norm of the corresponding column of $\boldsymbol{H}$, namely, $D_i = \|\boldsymbol{H}(:,i)\|$. For the case of the rendezvous problem, $a\delta u$ tends to exceeds the other state vector components $\boldsymbol{x}$, which is why normalization is essential. According to [11], the conditional number of the measurement mapping matrix has the following relationship:

$$\frac{\|\delta\boldsymbol{x}'\|}{\|\boldsymbol{x}'\|} \leq cond(\boldsymbol{A}')\frac{\|\delta\boldsymbol{b}'\|}{\|\boldsymbol{b}'\|} \tag{43}$$

Therefore $cond(\boldsymbol{A}')$ can be the metrics of sensitivity; from errors of relative measurement to those of relative estimation. When computation is performed in double-precision, if $cond(\boldsymbol{A}')$ is less than 10^{16} , the system should be practically observable since the significant digits of double-precision are 15 – 16. The smaller the $cond(\boldsymbol{A}')$, the more accurate the expected solution.

To confirm the observability of several basic relative motions, simple simulations are performed and Table 2 lists the ROEs of the relative motions, while the orbit of each spacecraft is propagated as a Keplerian problem for an orbital period and the interval of measurements is 600 s. At each simulation time, all accumulated measurements are used to compute $\boldsymbol{A}'$, whereupon the profiles of $rand(\boldsymbol{A}')$ and $cond(\boldsymbol{A}')$ are plotted. The results are shown in Figure 8.

Table 2. List of Relative Orbital Elements for Observability Analysis

ROE	Case A V-bar hold	Case B Coelliptic approach	Case C Football orbit	Case D Non-coelliptic approach
$a\delta a$	0 km	1 km	0 km	1 km
$a\delta e_x$	0 km	0 km	1 km	1 km
$a\delta e_y$	0 km	0 km	0 km	0 km
$a\delta i_x$	0 km	0 km	0 km	0 km
$a\delta i_y$	0 km	0 km	0 km	0 km
$a\delta u$	30 km	30 km	30 km	30 km

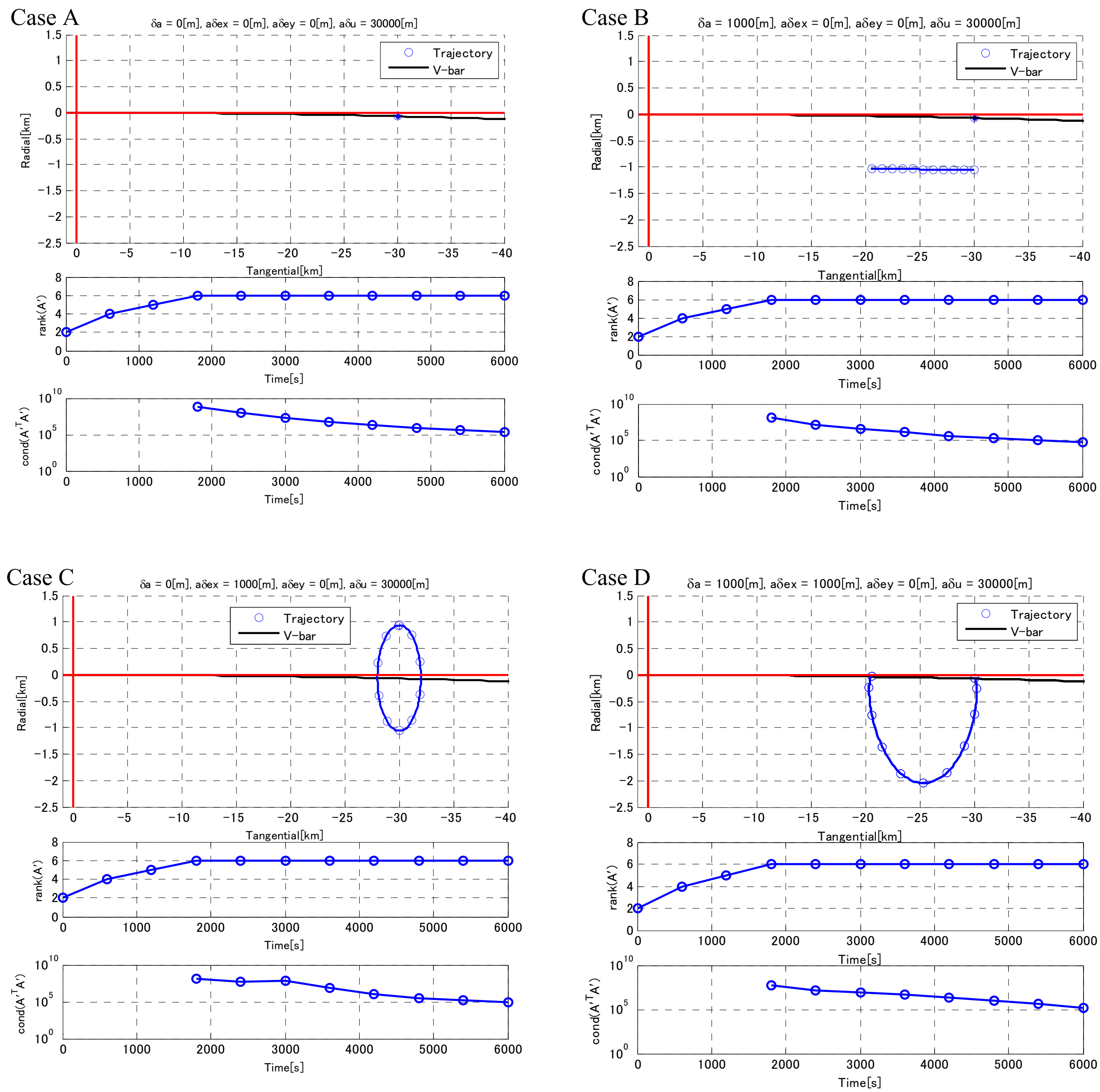

Figure 8. Observability of Basic Relative Motions (Relative Orbit in RTN, Rank and Cond)

In all cases, the rank profiles reach 6 (full-rank) with four measurements, which means that even if the system dynamics are modeled as a Keplerian problem, the AON is observable. A minimum of four measurements are necessary to produce observability since in-plane motion can be parameterized with four components of relative orbital elements: $\delta a, \delta e_x, \delta e_y, \delta u$. It should also be noted that even the relative motion is simple v-bar hold (Case A), the system is observable, and the observability differs little from other more complex relative motions which trigger greater variation in LOS angle profiles.

To confirm understanding whereby AON observability is obtained by transforming coordinates between the CVL and RTN frames, a simulation which excludes transformation is conducted, while the case including J2 effects is also simulated; the results of which are shown in Figure 9.

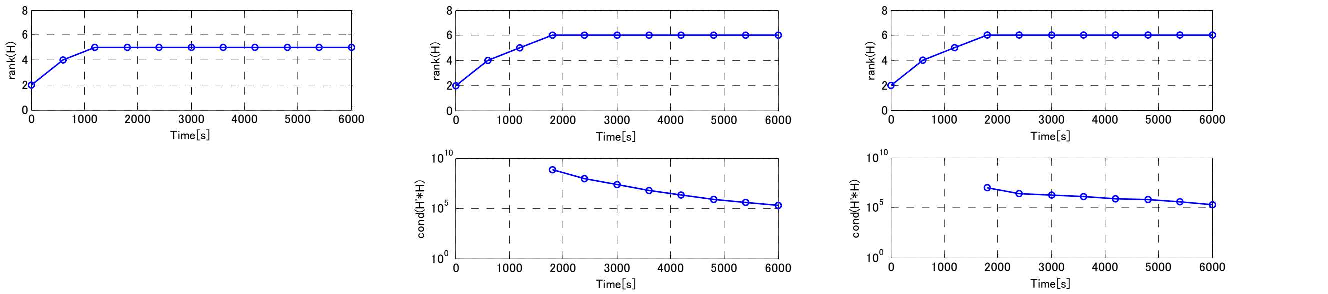

Figure 9. How CVL-RTN Transformation and J2 Affect Observability (left: CW propagation without CVL-RTN transformation, middle: Keplerian propagation with the transformation, right: add J2 perturbation)

As seen in Figure 9 (left), the rank reaches 5 (not full-rank) when relative motion is propagated by the CW equations and the CVL-RTN coordinate transformation is neglected, which means CVL-RTN transformation is essential for AON observability. Based on a comparison of the condition number of Figure 9 (middle and right), it can be seen that the J2 term slightly improves observability.

As shown in Figure 6 (right), the separation between the CVL and RTN soars with increasing along-track separation, which means the shorter the along-track separation, the poorer the observability. To confirm this intuitive assumption, the condition numbers after a single orbital revolution at the v-bar hold point are computed for various along-track distances and the results are shown in Figure 10.

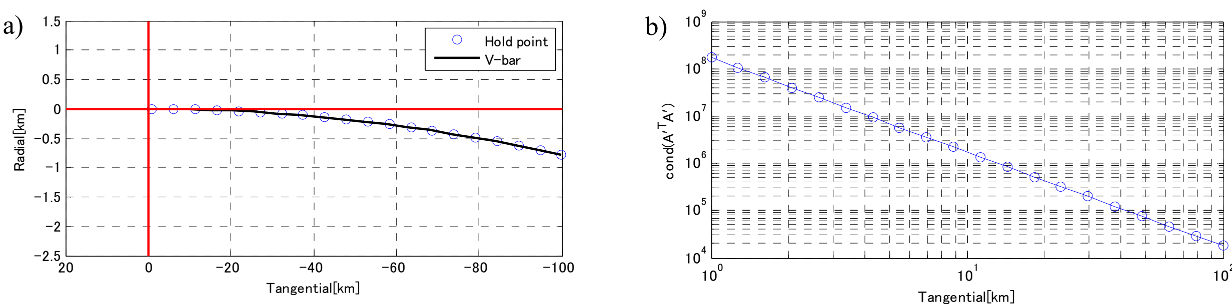

Figure 10. Along-Track Separation and Observability (left: computed location for each along-track separation, right: condition numbers)

As clearly shown in Figure 10 (right), the along-track separation has a linear relationship with the condition number on the log-log plot, which means that as the chaser approaches the target, the sensitivity from relative measurement errors to relative estimation errors soars. Accordingly, even if sufficient observability of the AON can be obtained in the far-range rendezvous, observability may decreases rapidly in the proximity rendezvous phase, whereupon proper maneuvers to actively stimulate observability might be necessary to sustain relative navigation accuracy.

6. Rendezvous Linear Covariance Analysis Formulation

There are generally two applicable methods used to evaluate dispersions of rendezvous navigation errors and control errors. One is the Monte Carlo method, and the other is linear covariance analysis. Linear covariance analysis techniques are designed to produce statistical results equivalent to a Monte Carlo simulation without performing hundreds or thousands of simulation runs and are convenient when assessing many different aspects of the rendezvous problem within a short period. In this work, the ROE based formulation of the rendezvous linear covariance analysis is developed based on the formulation of Geller [12].

The preceding equations are linearized around reference relative orbital elements $\overline{\boldsymbol{x}}$.

$$\begin{aligned} \delta\boldsymbol{x} &= \boldsymbol{x} - \overline{\boldsymbol{x}} \\ \delta\hat{\boldsymbol{x}} &= \hat{\boldsymbol{x}} - \overline{\boldsymbol{x}} \end{aligned} \tag{44}$$

where true state dispersions from the reference are $\delta\boldsymbol{x}$ and the navigation state dispersions from the reference are $\delta\hat{\boldsymbol{x}}$. Next, we define the augmented state vector $\boldsymbol{X}$ and its covariance $\boldsymbol{C}_A$ of the true state and navigation state dispersions:

$$\begin{aligned} \boldsymbol{X} &= \begin{pmatrix} \delta\boldsymbol{x} \\ \delta\hat{\boldsymbol{x}} \end{pmatrix} \\ \boldsymbol{C}_A &= \boldsymbol{E}[\boldsymbol{X}\boldsymbol{X}^T] \end{aligned} \tag{45}$$

The propagation, update, and correction for impulsive maneuvers of the augmented state vector can be formulated as:

$$\begin{aligned} \boldsymbol{X}_{k+1} &= \boldsymbol{F}_k \boldsymbol{X}_{k+1} + \boldsymbol{W}\boldsymbol{w}_k && \text{: Propagating} \\ \boldsymbol{X}_k^+ &= \boldsymbol{A}_k \boldsymbol{X}_k^- + \boldsymbol{B}_k \boldsymbol{\nu} && \text{: Update} \\ \boldsymbol{X}_k^+ &= \boldsymbol{D}_k \boldsymbol{X}_k^- + \boldsymbol{N}_k \varDelta\boldsymbol{w}_k && \text{: Impulsive maneuver} \end{aligned} \tag{46}$$

$$\begin{aligned} \boldsymbol{F}_k &= \begin{pmatrix} \boldsymbol{\Phi} & 0 \\ 0 & \widehat{\boldsymbol{\Phi}} \end{pmatrix}, \boldsymbol{W} = \begin{pmatrix} \boldsymbol{I} \\ \boldsymbol{0} \end{pmatrix} \\ \boldsymbol{A}_k &= \begin{pmatrix} \boldsymbol{I} & \boldsymbol{0} \\ \widehat{\boldsymbol{K}}\boldsymbol{H} & \boldsymbol{I} - \widehat{\boldsymbol{K}}\widehat{\boldsymbol{H}} \end{pmatrix}, \boldsymbol{B}_k = \begin{pmatrix} \boldsymbol{0} \\ \widehat{\boldsymbol{K}} \end{pmatrix} \\ \boldsymbol{D}_k &= \begin{pmatrix} \boldsymbol{I} & B\Delta\hat{\boldsymbol{G}}_{\hat{\boldsymbol{x}}} \\ \boldsymbol{0} & \boldsymbol{I} + \widehat{\boldsymbol{B}}\Delta\hat{\boldsymbol{G}}_{\hat{\boldsymbol{x}}} \end{pmatrix}, \boldsymbol{N}_k = \begin{pmatrix} \boldsymbol{B} \\ \boldsymbol{0} \end{pmatrix} \end{aligned} \tag{47}$$

where, $\Delta\hat{\boldsymbol{G}}_{\hat{\boldsymbol{x}}}$ is a Jacobean matrix of the onboard control algorithm $\Delta\hat{\boldsymbol{g}}(\hat{\boldsymbol{x}}, t)$ as follows:

$$\Delta\boldsymbol{v}^{RTN} = \Delta\hat{\boldsymbol{g}}(\hat{\boldsymbol{x}}, t) \tag{48}$$

$$\Delta\hat{\boldsymbol{G}}_{\hat{\boldsymbol{x}}} = \frac{\partial}{\partial\hat{\boldsymbol{x}}}\Delta\hat{\boldsymbol{g}}(\hat{\boldsymbol{x}}, t)$$

and the Jacobean can be computed by numerical differentiation of $\Delta\hat{\boldsymbol{g}}(\hat{\boldsymbol{x}}, t)$. The propagation, update, and correction for the impulsive maneuver of the linearized covariance matrix can be formulated as:

$$\begin{aligned}
&\boldsymbol{C}_{Ak+1} = \boldsymbol{F}_k\boldsymbol{C}_{Ak}\boldsymbol{F}_k^T + \boldsymbol{W}\boldsymbol{Q}\boldsymbol{W}^T && \text{: Propagating} \\
&\boldsymbol{C}_{Ak}^{+} = \boldsymbol{A}_k\boldsymbol{C}_{Ak}^{-}\boldsymbol{A}_k^T + \boldsymbol{B}_k\boldsymbol{R}\boldsymbol{B}_k^T && \text{: Update} \\
&\boldsymbol{C}_{Ak}^{+} = \boldsymbol{D}_k\boldsymbol{C}_{Ak}^{-}\boldsymbol{D}_k^T + \boldsymbol{N}_k\Delta\boldsymbol{Q}\boldsymbol{N}_k^T && \text{: Impulsive maneuver}
\end{aligned} \tag{49}$$

Using this equation, the time evolution of the covariance can be computed and the overall closed-loop performance can be evaluated by examining the covariance of the true state dispersions $\boldsymbol{P}_{true}$ and that of the true navigation state errors $\boldsymbol{P}_{nav}$. They can be extracted as follows:

$$\begin{aligned}
\boldsymbol{P}_{true} &= E[\delta\boldsymbol{x}\delta\boldsymbol{x}^T] = (\boldsymbol{I} \quad \boldsymbol{0})\boldsymbol{C}_A(\boldsymbol{I} \quad \boldsymbol{0})^T \\
\boldsymbol{P}_{nav} &= E[(\delta\hat{\boldsymbol{x}} - \delta\boldsymbol{x})(\delta\hat{\boldsymbol{x}} - \delta\boldsymbol{x})^T] = (-\boldsymbol{I} \quad \boldsymbol{I})\boldsymbol{C}_A(-\boldsymbol{I} \quad \boldsymbol{I})^T
\end{aligned} \tag{50}$$

Using the linear covariance analysis framework, the time evolution of the covariance of the true state dispersions and true navigation state errors can be computed immediately without hundreds of Monte Carlo runs.

7. Far-Range Trajectory Design

The far-range rendezvous trajectory should be designed with the following points in mind. First, passive abort should be safe. Second, the observability of the AON should be confirmed and third, the fuel consumption should be feasible.

The AON has been utilized as the primary method of relative navigation for various cooperative rendezvous missions from former GEMINI to recent Space Shuttles. There are two typical types of rendezvous trajectory considering the AON. One is the Stable-Orbit Rendezvous type, which accommodates a V-bar hold point in the nominal trajectory, and the other is the Dual-Coelliptic Rendezvous (DCR) type, in which the chaser spacecraft approaches along the coelliptic orbit without a V-bar hold point. Illustrations of these rendezvous trajectories are shown in Figure 11.

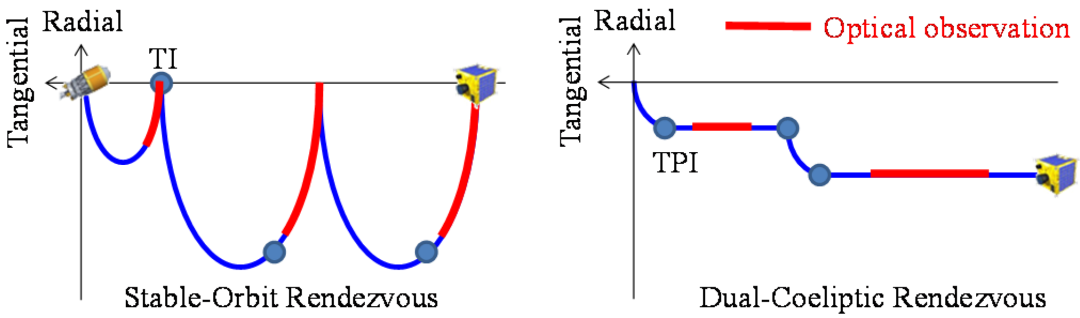

Figure 11. Typical Rendezvous Trajectory Considering AON (left: SOR, right:DCR)

According to Goodman [13], the nominal approach trajectory of the space shuttle was double coelliptic rendezvous (DCR) until 1983, and subsequently stable orbit rendezvous (SOR).

The strong point of the SOR is the fact that the chaser spacecraft can remain at the V-bar hold point and adjust the arrival time arbitrarily. Some space missions like the rendezvous to International Space Station (ISS) require a strict and precise arrival time at the destination since ISS must engage in many preparations to welcome the visiting spacecraft and manage the working time of astronauts. The weak point of the SOR is the difficulty in ensuring passive abort (PA) safety, since the hold point is located on the V-bar and naturally propagated orbit may result in a collision with the target.

Conversely, the strong point of the DCR is PA safety, since the altitude of the DCR approach trajectory is always lower than that of the target. The drawback is the limitation imposed on the arrival time adjustment. Despite the fact the arrival time can somehow be adjusted by selecting the proper relative altitude of two coelliptic orbits, its capability remains finite.

One of the specific characteristics of a non-cooperative rendezvous is the uncertainty of relative navigation and a non-cooperative target lacks any navigation aids such as laser retroreflectors or markers to support reliable relative navigation. Accordingly, the risk of failing to track the target and losing it during a critical phase of the rendezvous is supposedly significantly higher than in the case of a cooperative rendezvous mission. Besides, a non-cooperative rendezvous mission does not usually impose any strict arrival time requirement, since the target is already dead and there is no way to prepare on the target side. With the above issues in mind, the DCR is supposed to be the proper selection for the nominal far-range rendezvous trajectory, since PA safety is key for a non-cooperative rendezvous mission.

8. Rendezvous Simulation Results

To demonstrate the relative navigation ideas and wide-ranging rendezvous trajectory selection, numerical simulations are conducted; the scope of which goes from the far-range rendezvous with an along-track separation of 70 km to the insertion into the 1 km V-bar point where MMN is supposed to initiate. The simulation cases described in Table 3 are selected by focusing on the following three points. One is the control accuracy of the V-bar point insertion trajectory, another is the navigation performance comparison between the DCR and SOR, and the other is how the selection of the navigation sensor types (VISCAM, IRCAM, and LIDAR) affect navigation performance.

Table 3. Rendezvous Simulation Cases Summary

	Approach orbit type	VISCAM	IRCAM	LIDAR (Range only)
Case A	DCR	✓	Not used	Not used
Case B	DCR	✓	✓	Not used
Case C	DCR	✓	✓	✓
Case D	SOR	✓	✓	Not used

Case B, in which the chaser carries a VISCAM and IRCAM and engages in a rendezvous along the DCR is the nominal simulation case. Case D is used to compare between the DCR and SOR. In Cases A and C, the effects of the selection of navigation sensor types on navigation performance are evaluated.

The simulation models are summarized in Table 4, while the orbit propagation of the truth model is performed by the Earth gravity field model with 20 degrees and order. The technical parameters of the VISCAM, IRCAM, and LIDAR are set referring to the specifications of existing spaceborne or commercial products. The target is modeled as a simple flat panel with optical properties as shown in Table 4. The guidance logic is the simple CW targeting to the reference trajectory [8] .

Table 4. Simulation Models Summary

Truth model orbit propagation	Low Earth Orbit Geopotential: JGM3 20×20 Drag, Solar radiation, Luni-Solar perturbations: not applied
VISCAM	Noise: 0.1deg random (1σ) f = 75, F = 1, 640×480 CCD camera
IRCAM	Noise: 0.1deg random (1σ) f = 75, F = 1, 640×480 IR camera
LIDAR (range only)	Noise: 10m random(1σ) Peak power = 1 MW Receiver diameter = 10 cm, Sensitivity = 0.4 A/W
Debris optical property	Modified Phong model k_d = 0.2, k_s = 0.5, n = 28
Navigation	EKF to estimate relative elements Initial error: $a\delta a$= 60 m $a\delta e_x$, $a\delta e_y$, $a\delta i_x$, $a\delta i_y$= 300 m $a\delta u$ = 3000 m
Guidance	CW targeting
Maneuver	Impulsive maneuver

The results of the linear covariance analysis of both Cases B and D are shown in Figure 12, while a close-up of V-bar insertion is shown in Figure 13. Figure 14 features the along-track navigation performance comparison between the DCR and SOR, while Figure 15 shows the along-track navigation performance for Cases A/B/C and the detectability profile of each sensor type.

The green points in Figure 12 reveal valid measurements. In far-range valid measurements are only available when the sun is visible and its direction favors strong reflection from the target. At a distance of around 16 km, the IRCAM starts to detect the target, from which valid measurements can be obtained regardless of the sun direction. The red ellipses reveal one sigma control dispersions; showing that the size of the dispersions shrink into the level of navigation error at the time when maneuvers are executed. In both cases of DCR and SOR, insertion into the 1 km V-bar point is performed with reasonable size of dispersions.

Figure 14 shows that the navigation error and its covariance of $a\delta u$ shrink into smaller values when valid measurements are obtained, and the navigation performance is refined as the chaser approaches the target in both DCR and SOR cases. Although the navigation performance of the DCR is slightly exceeds that of SOR, the difference is minor and means the DCR is not inferior or even superior to the SOR in terms of AON observability. Selecting of the DCR as the nominal far-range rendezvous trajectory seems reasonable in terms of both PA safety and observability.

From Figure 15(right) it can be seen that the VISCAM can detect the target, even at a relatively long distance, e.g. 70km, but it is not available when the target is in eclipse or the direction of the sun is unfavorable. Conversely, the IRCAM starts to detect the target at a distance of around 16 km and continues stable detection regardless of eclipses. The LIDAR starts to detect the target at a distance of around 30 km and continues stable detection. Note that the detectability results are computed assuming the hardware specified in Table 4, and will change dramatically once the specifications are modified.

From Figure 15(left) the effectiveness of the IRCAM and LIDAR can be seen. In Case A, a relatively large navigation error in the along-track direction remains, even when the relative distance goes under 10 km due to intermittent available measurements. Conversely, owing to continuous stable measurements by the IRCAM, navigation error in Case B shrinks as the chaser approaches when relative distance is less than 16 km. In Case C, the navigation error improves dramatically when the LIDAR starts to detect the target by incorporating direct range information into the navigation filter. This result shows that the direct range information significantly boosts the uncertainty of along-track distance inherent to the AON, and the LIDAR type sensor is effective for safety; especially in proximity and where the AON observability tends to be poor.

9. Conclusions

This work addresses the design of the relative navigation and the rendezvous trajectory for a non-cooperative rendezvous. It was mainly motivated by the ADR mission with the EDT system which is a reference design mission investigated in JAXA.

Navigation sensors applicable to non-cooperative targets are investigated and detectability analysis models are developed. The VISCAM and IRCAM are selected as the nominal sensor combination, the LIDAR is considered optional and the navigation sensor usage matrix is designed. During a far-range rendezvous the AON is utilized as the primary navigation source, and at a distance of around 1 km, it switches to the MMN.

The filter design of angles-only navigation (AON) is studied. It is claimed that processing LOS angle measurements of natural relative orbit can make the system observable when coordinate transformation between the orthogonal RTN and CVL frames is properly modeled. The observability dramatically declines as the chaser approaches the target. Besides, the mathematical framework for rendezvous linear covariance analysis, in which the relative state is parameterized in terms of relative orbital elements, is presented.

Based on the relative navigation sensor analysis, a suitable trajectory design for a non-cooperative rendezvous was discussed and following a trade-off study, the DCR was selected as the nominal approach trajectory while prioritizing passive abort safety, since relative navigation to a non-cooperative target is sometimes considered unreliable.

Rendezvous simulations were performed to demonstrate the navigation and trajectory design for the reference mission and it was confirmed that selecting the DCR as the nominal trajectory was reasonable in terms of safety and navigation performance. In the proximity rendezvous phase, the IRCAM can significantly facilitate stable navigation and suppression of along-track navigation errors. Moreover, the LIDAR is also effective for safety, particularly in proximity and where the AON observability tends to be poor. If the LIDAR remains affordable, its actual use may be considered.

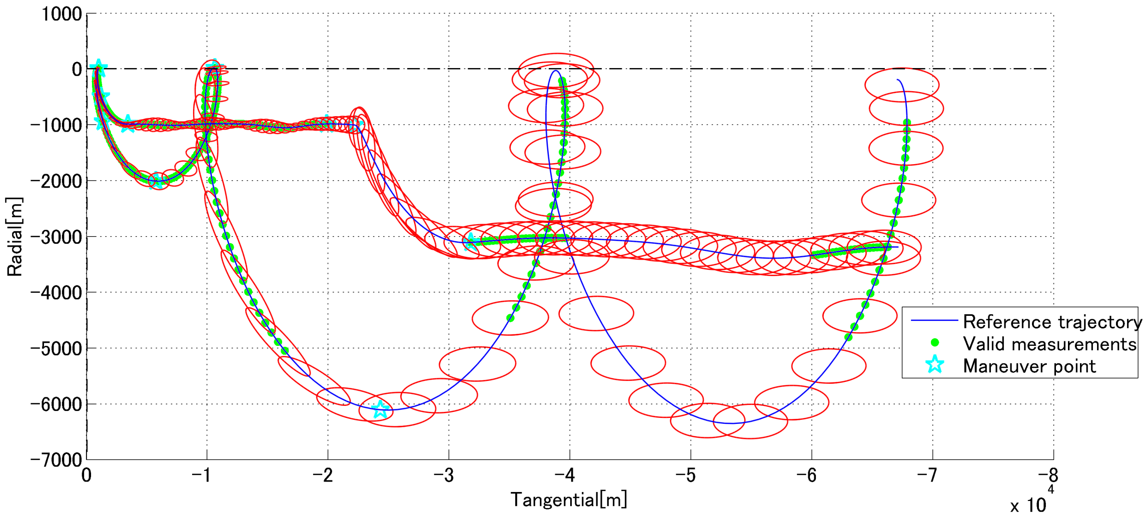

Figure 12. Control Error Dispersions by Linear Covariance Analysis for DCR and SOR

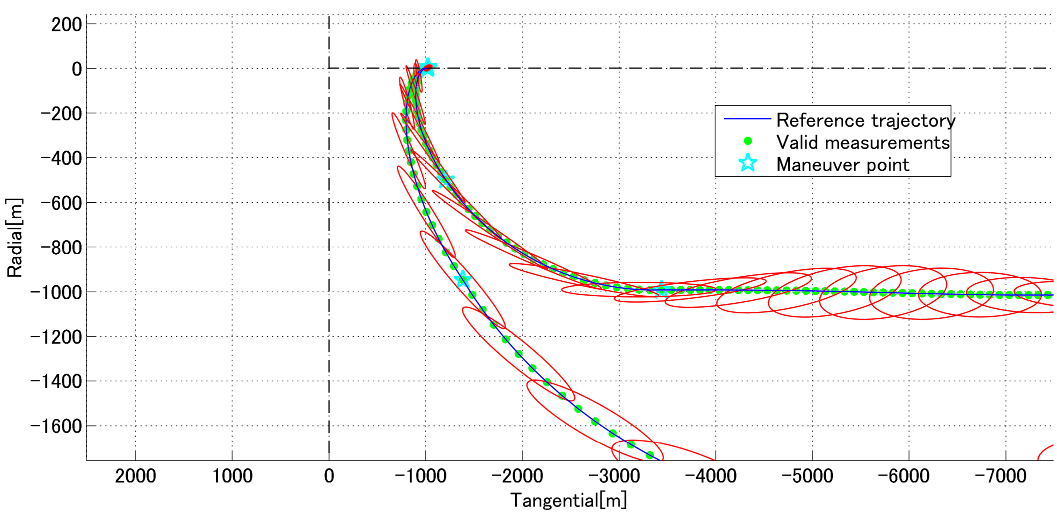

Figure 13. Control Error Dispersions by Linear Covariance Analysis (close-up)

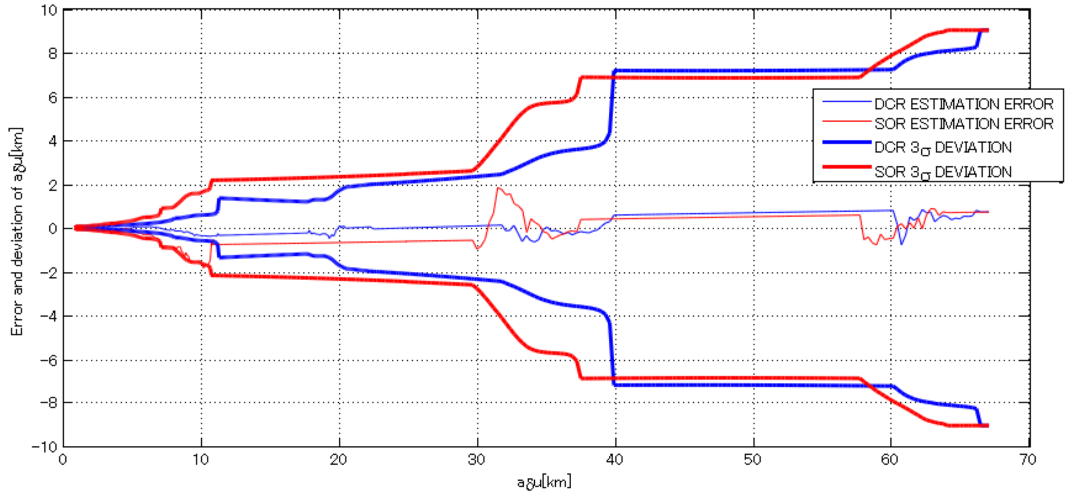

Figure 14. Along-Track Navigation Performance Comparison between DCR and SOR

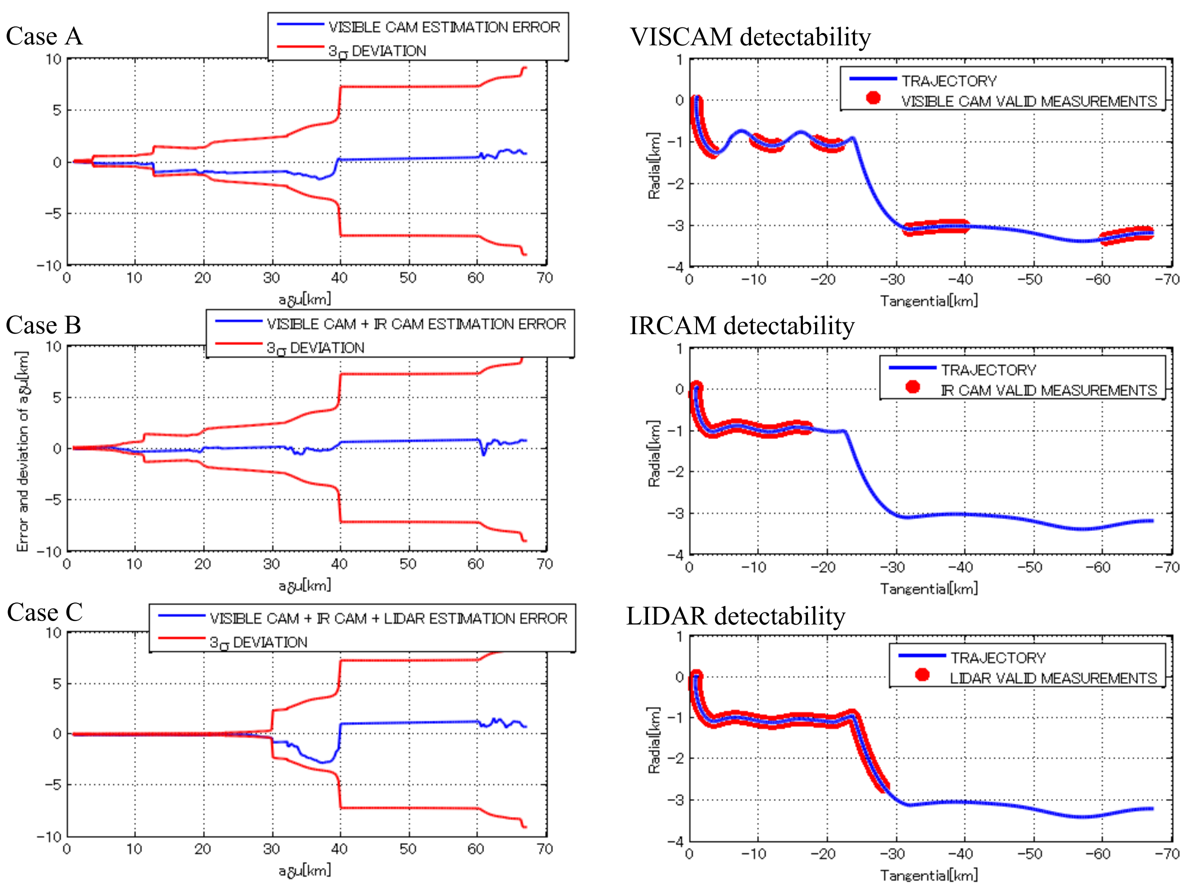

Figure 15. Along-Track Navigation Performance for Case A/B/C (left) and Detectability of Each Sensor Type (right)

10. References

[1] Liou, J.-C., "An active debris removal parametric study for LEO environment remediation.", Advances in Space Research Volume 47, Issue 11, pp. 1865-1876, 2011.

[2] Kawamoto, S., Makida, T., Sasaki, F., Okawa, Y., Nishida, S., "Precise numerical simulations of electrodynamic tethers for an active debris removal system.", Acta Astronautica, Volume 59, Issues 1–5, pp. 139-148, 2006.

[3] Taromaru, Y., Hirose, C., Mori, S., Horii, M., Yamamoto, Y., Aoki, S., and Isobe, S. "Observation of space debris by the Kamisaibara radar system.", Proceedings of the 4th European Conference on Space Debris, pp. 18-20, 2005

[4] Kahle R., Weigel M., Kirschner M., Spiridonova S., Kahr E., Letsch K., "Relative Navigation to Non-Cooperative Targets in LEO: Achievable Accuracy from Radar Tracking Measurements", 5th International Conference on Spacecraft Formation Flying Missions and Technologies, 2011

[5] Leinz, M. R., Chen, C. T., Beaven, M. W., Weismuller, T. P., Caballero, D. L., Gaumer, W. B., and Lundgren, M. A., "Orbital express autonomous rendezvous and capture sensor system (ARCSS) flight test results.", Proc. SPIE 6958, Sensors and Systems for Space Applications II, 69580A, 2008.

[6] Lafortune, E. P., and Willems, Y. D., "Using the modified phong reflectance model for physically based rendering.", Report CW, 197, 2-4, 1994.

[7] Woffinden, D. C., and Geller, D. K., "Observability criteria for angles-only navigation.", Aerospace and Electronic Systems, IEEE Transactions on, 45(3), pp.1194-1208, 2009.

[8] Clohessy, W. H., and Wiiltshire, R. S., "Terminal guidance system for satellite rendezvous.", Journal of the Aerospace Sciences, 27(9), pp.653-658, 1960.

[9] Woffinden, D. C., and Geller, D. K., "Optimal orbital rendezvous maneuvering for angles-only navigation.", Journal of guidance, control, and dynamics, 32(4), pp.1382-1387, 2009.

[10] Gaias, G., D'Amico, S., and Ardaens, J. S., "Angles-Only Navigation to a Noncooperative Satellite Using Relative Orbital Elements.", Journal of Guidance, Control, and Dynamics, 37(2), pp.439-451, 2014.

[11] Gibbs, B. P., "Advanced Kalman filtering, least-squares and modeling: a practical handbook.", John Wiley & Sons, 2011.

[12] Geller, D. K., "Linear covariance techniques for orbital rendezvous analysis and autonomous onboard mission planning.", Journal of Guidance, Control, and Dynamics, 29(6), 1404-1414., 2006.

[13] Goodman, J. L., “History of space shuttle rendezvous and proximity operations.”, Journal of Spacecraft and Rockets, 43(5), pp.944-959, 2006.